Detailed Multi-dimensional Modeling of Direct Internal Reforming Solid Oxide Fuel Cells

K. Tseronis[1], I.S. Fragkopoulos[1], I. Bonis[1], C. Theodoropoulos[1]*

[1] School of Chemical Engineering and Analytical Science, University of Manchester, Manchester M13 9PL, UK

Abstract

Fuel flexibility is a significant advantage of solid oxide fuel cells (SOFCs) and can be attributed to their high operating temperature. Here we consider a direct internal reforming solid oxide fuel cell setup in which a separate fuel reformer is not required. We construct a multidimensional, detailed model of a planar solid oxide fuel cell, where mass transport in the fuel channel is modeled using the Stefan-Maxwell model, whereas the mass transport within the porous electrodes is simulated using the Dusty-Gas model. The resulting highly nonlinear model is built into COMSOL Multiphysics, a commercial computational fluid dynamics software, and is validated against experimental data from the literature. A number of parametric studies is performed to obtain insights on the direct internal reforming solid oxide fuel cell system behavior and efficiency, to aid the design procedure. It is shown that internal reforming results in temperature drop close to the inlet and that the direct internal reforming solid oxide fuel cell performance can be enhanced by increasing the operating temperature. It is also observed that decreases in the inlet temperature result in smoother temperature profiles and in the formation of reduced thermal gradients. Furthermore, the direct internal reforming solid oxide fuel cell performance was found to be affected by the thickness of the electrochemically-active anode catalyst layer, although not always substantially, due to the counter-balancing behavior of the activation and ohmic overpotentials.

Keywords: DIR-SOFC, Dusty-Gas/Stefan-Maxwell Coupling, Multidimensional Modeling, Parallel H_2 and CO Electro-oxidation

1 Introduction

A method for obtaining the hydrogen required for the solid oxide fuel cell (SOFC) operation, is through catalytic steam reforming (CSR) of methane or natural gas. Natural gas is one of the most widely available light hydrocarbon fuels. It is a fuel mixture typically consisting of methane and smaller amounts of higher hydrocarbons, such as ethane, propane, butane, and of nitrogen. CSR is typically carried out between 700 °C and 900 °C [1], therefore, it is compatible with the high SOFC operating temperatures. Additionally, SOFC anodes typically comprise of metal catalysts that promote the CSR reaction. The general reforming reaction of a hydrocarbon can be written as:

$$C_nH_mO_p + (n - p)H_2O \rightarrow nCO + (n - p + m/2)H_2 \, , \Delta H^o > 0 \tag{1}$$
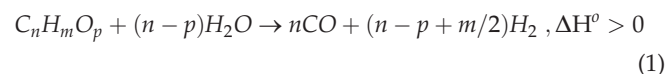
Methane, which is the most common fuel in internal reforming SOFC (IR-SOFC) systems, due to the higher effi-ciency that can be achieved from its use [2,3], reacts with steam to produce hydrogen (H_2) and carbon monoxide (CO) in the methane-steam reforming (MSR) reaction:

$$CH_4 + H_2O \rightarrow CO + 3H_2 \, , \Delta H^o_{(1073K)} = 242 \text{ kJ mol}^{-1} \tag{2}$$
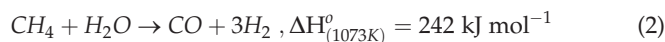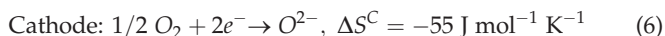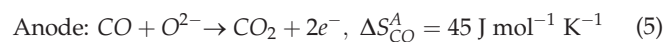
The MSR reaction is thermodynamically favored at high temperatures and low pressures, since the forward reaction results in volume increase [1]. At the same time, CO further reacts with steam (H_2O) to generate additional hydrogen and carbon dioxide (CO_2) in the water-gas shift (WGS) reaction:

$$CO + H_2O \leftrightarrow CO_2 + H_2 \, , \Delta H^o_{(1073K)} = -38.6 \text{ kJ mol}^{-1} \tag{3}$$
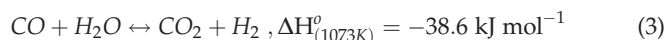
As can be seen from reactions (2) and (3), MSR is a highly endothermic reaction, whereas the WGS, as well as the electro-

[*] Corresponding author, k.theodoropoulos@manchester.ac.uk

chemical oxidation, are exothermic reactions [4, 5]. In our model, in addition to the aforementioned reactions, the simultaneous electrochemical oxidation of H_2 and CO at the anode is taken into account as can be seen in Figure 1. Therefore, the electrochemical reactions at the active layers of the anode and cathode electrodes are as follows:

Anode: $H_2 + O^{2-} \rightarrow H_2O + 2e^-$, $\Delta S_{H_2}^A = 25$ J mol^{-1} K^{-1} (4)

Anode: $CO + O^{2-} \rightarrow CO_2 + 2e^-$, $\Delta S_{CO}^A = 45$ J mol^{-1} K^{-1} (5)

Cathode: $1/2\, O_2 + 2e^- \rightarrow O^{2-}$, $\Delta S^C = -55$ J mol^{-1} K^{-1} (6)
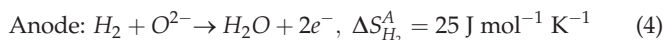
Based on these half-cell reactions, the overall electrochemical reactions are the following:

$$H_2 + \frac{1}{2}O_2 \leftrightarrow H_2O \qquad (7)$$

$$CO + \frac{1}{2}O_2 \leftrightarrow CO_2 \qquad (8)$$

The entropy change is evaluated separately for each electrochemical half-cell reaction [6, 7], since the overall reaction of a SOFC does not provide information on how the heat is distributed among each electrode [8]. Using this approach the temperature distribution in the solid parts of the SOFC can be evaluated more accurately.

Two operating parameters that are commonly used to characterize reforming systems are the steam to carbon ratio (S/C) and the stoichiometric ratio (SR) [9]. S/C is defined as the mole fraction of steam in the anode fuel to all combustible species mole fractions and is given by:

$$S/C = \frac{\dot{n}_{H_2O}}{\dot{n}_C} \qquad (9)$$

SR is defined as the amount of oxygen in the inlet of the system over the amount of oxygen needed to achieve complete combustion and is given by:

$$SR = \frac{\dot{n}_{O_2}}{\dot{n}_{O_2,\ stoichiometric}} \qquad (10)$$

A sufficient amount of steam is necessary in the reformer, in order to fulfil the reforming reaction requirements. Previous studies on methane reforming in SOFCs have shown that a S/C ratio higher than 2 guarantees that carbon formation does not occur in the SOFC [10]. However, a very high S/C ratio can prove to be an inefficient choice, as it would dilute the hydrogen in the fuel channel, lowering the electrical efficiency of the cell. Therefore, the S/C ratio is usually kept below 3.5 [11].

Some of the benefits of CSR of hydrocarbons in SOFCs are the production of hydrogen *in situ*, the higher overall efficiencies and the simplicity of the resulting system in the case of internal reforming (IR) due to the combined reforming and electrochemical processes [12].

One of the main downsides of MSR in IR-SOFCs is the formation of steep temperature gradients within the cell, due to the highly endothermic reforming reaction, which results in thermal stresses that can lead to structural failures. Such gradients are formed mainly at the inlet of the fuel channel where the highly endothermic MSR reaction rate is large, due to the higher methane concentration, resulting in much lower temperatures than the feed temperature. As methane flows in the fuel channel, methane concentration decreases, while hydrogen concentration respectively increases, causing the exothermic electrochemical (oxidation) reactions to dominate the MSR reaction, resulting in a temperature increase downstream in the cell. Another limitation of MSR is that, despite their relatively high tolerance in carbon, the anode electrode catalysts can suffer from carbon deposition, which can result in its deactivation in the long term.

To alleviate the aforementioned limitations some degree of upstream fuel processing, including recirculation, can be used. Natural gas can be fed in a pre-reforming reactor along with a fraction of the outlet anode stream that is recirculated from the SOFC, in order to produce a fuel stream that is rich in H_2 and CO and dilute in hydrocarbons. The decreased methane (CH_4) concentration means that the S/C ratio is increased, and the increased H_2 and CO concentrations mean that a higher current density is observed at the inlet, which consequently results in the production of more steam through the electrochemical reactions. Higher S/C ratios and current densities have been found to decrease the rate of carbon formation [12]. In addition, the generated temperature gradients in the SOFC become smaller, due to the increase in the relative rate
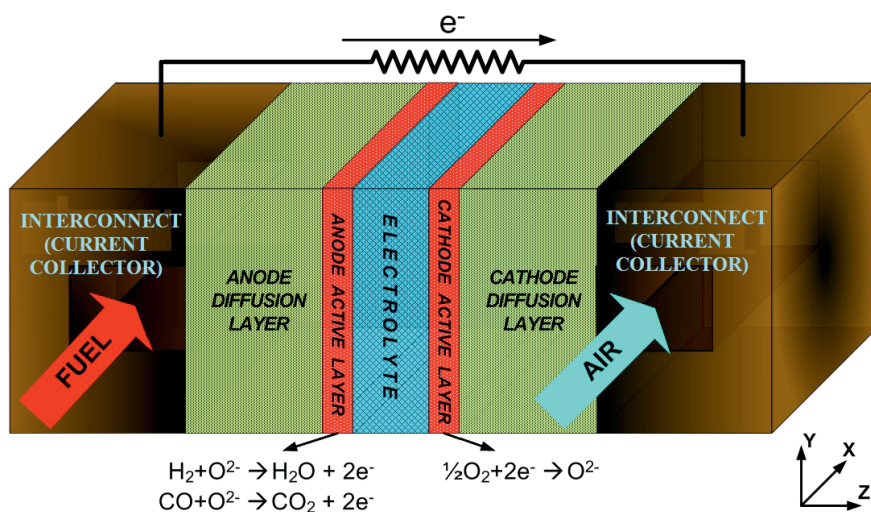

Fig. 1   Schematic representation of the basic operation principles of a DIR-SOFC.

of the exothermic electrochemical reactions versus the rate of the endothermic reforming reaction.

In this work, the Dusty-Gas model (DGM) is employed for the simulation of mass transport in the porous anode and cathode electrodes of a direct internal reforming solid oxide fuel cell (DIR-SOFC) system. Several studies have been conducted to review and compare the mass transport approaches which can be followed for accurate SOFC modeling and they concur that DGM can be deemed accurate and dependable [13–16]. Although the merits of DGM are highly held of in the SOFC community, to the best of our knowledge only a handful of works exist in the literature employing DGM for IR-SOFC in button [17] and planar configurations [18–20]. The closest work to the one discussed here is Janardhanan and Deutschmann's [18] who simulate a planar Membrane Electrode Assembly (MEA) SOFC with an iterative, fixed-point algorithm. Here, although a MEA is not applied, the governing partial differential equations (PDEs) are fully coupled and solved simultaneously using a commercial computational fluid dynamics (CFD) package, yielding a computationally efficient and flexible model. In [18] charge transfer takes place only at the electrode-electrolyte interface considering the triple phase boundaries (TPBs) as 1-D boundaries, while here the TPBs are taken into consideration as finite 2-D zones in the anode electrode. Furthermore, this study takes into account the electrochemical oxidation of both H_2 and CO at the TPB of the anode.

Following the approach we introduced for the first time in [21] for anode SOFC simulations, and then extended on entire system SOFC simulations in [22], here the DGM is coupled with the Stefan-Maxwell model (SMM) achieving higher accuracy for mass transport simulations in DIR-SOFCs. Such a detailed model can be used for the investigation of the effect of various parameters on the SOFC performance, targeting robust design and control of DIR-SOFC systems. Such detailed models can be used directly in conjunction with model reduction techniques in the context of optimisation [23, 24] and control [25, 26], achieving both accurate and robust design and operation.

This paper is organised as follows: the various approaches to SOFC fuel processing are presented in Section 2; in Section 3, the developed model is described in terms of reaction kinetics, governing PDEs and boundary conditions for the phenomena taken into consideration (mass, energy and charge transport) and domain considered. In Section 4, the constructed model is validated against experimental results available in literature. Furthermore, results obtained from base case simulations are presented and a parametric investigation is undertaken. In Section 5, the conclusions are discussed.

2 Approaches to SOFC Fuel Processing

SOFC systems typically obtain the hydrogen required for their operation from a hydrocarbon-based fuel source. Alcohols, such as methanol or ethanol, and hydrocarbons, such as

natural gas, are usually reformed into a hydrogen-rich synthesis gas by various methods. The most representative methods for this purpose are CSR, partial oxidation (POX) and autothermal reforming (ATR) [3, 27]. The fuel can be converted and reformed externally to the SOFC stack by external reforming (ER) or internally in the SOFC anode compartment by IR. ER requires an external heat source, such as a burner or hot waste gas and a fixed bed reactor. IR utilizes the heat release from the fuel electrochemical oxidation reactions by providing a convenient and efficient configuration for energy transfer between heat source and heat sink, simultaneously lowering the air cooling requirements of the SOFC [3].

There are two main approaches to IR within a SOFC, indirect internal reforming (IIR) and direct internal reforming (DIR). In the former approach, the reformer section is physically separated from the SOFC, but in close thermal contact with the anode, in order to make use of the SOFC stack released heat. In the latter approach, the hydrocarbon fuel mixture is fed directly into the anode fuel channel and the reforming reaction occurs there [10].

The two main advantages of CSR over POX and ATR processes are that it produces a high composition hydrogen mixture without dilution of the product stream and that it operates with a high fuel conversion efficiency (85%–95%) [3]. In contrast to the above, POX offers compactness, fast start-up and rapid dynamic response, but sacrifices fuel conversion efficiency. ATR, on the other hand, shares some of the features of CSR and POX technologies. The major difference between CSR, POX and ATR processes is the mechanism for providing the thermal energy required for the endothermic reforming reactions [3]. In this work, a DIR approach is going to be used for the developed IR-SOFC model.

2.1 Direct Internal Reforming

In DIR, the reforming reactions take place within the anode of the SOFC. This is feasible, since the high operating temperatures of SOFCs in combination with the nickel content of the anode electrodes provide sufficient activity for the MSR (2) and WGS (3) reactions [28]. In DIR-SOFC systems, there is very good system integration, because the steam produced from the hydrogen oxidation electrochemical reaction can be used directly in the reforming reaction. Additionally, the heat released in the DIR-SOFC can provide the heat for the MSR reaction. The need for SOFC cooling is usually satisfied by flowing excess air through the cathode air channel, but in DIR-SOFCs this is not necessary, because of the endothermic reforming reaction [10, 28]. Moreover, due to the ongoing hydrogen consumption by the electrochemical reactions, the equilibrium of the MSR reaction (2) is further shifted to the right, increasing the methane conversion and leading to a more evenly distributed load of hydrogen [10].

DIR has the advantage of eliminating the requirement for upstream processing without using a separate fuel reformer, as is the case for IIR, thus simplifying the overall SOFC system design, hence minimising its cost, size and complexity. Another

benefit of DIR over IIR is that in DIR the conversion of CH_4 to H_2 is promoted to a much larger extent than in IIR [10].

A DIR related drawback, as already mentioned, is the carbon formation on the anode electrode that not only deactivates the catalytic active sites, but can also damage the cell through delamination or nickel dusting leading to reduced SOFC performance [10, 29]. This problem can be alleviated by increasing the S/C ratio of the inlet fuel mixture to an amount greater than the stoichiometric requirement of reaction (2). However, the amount of steam necessary for carbon-free operation is not an easy choice, as in addition to the suppression of coke formation, S/C ratio can also affect the equilibrium yield of hydrogen. As the S/C ratio is increased, the hydrogen yield decreases. Furthermore, high S/C-ratios can cause nickel oxidation, which can lead to severe damaging of the cell through the alteration of the lattice structure [30, 31]. Increasing extensively the S/C ratio can also have a negative effect in the overall system efficiency, since the energy requirements for steam generation are also increased. Advanced anode materials that allow DIR at low steam/carbon ratios can offer an alternative approach with significant benefits [28].

Another negative aspect, mostly affecting the high temperature DIR-SOFCs, is the strong cooling effect caused by the highly endothermic MSR reaction. It has been demonstrated that almost all CH_4 is reformed within a small distance from the anode inlet [10, 28]. This can result in very steep temperature gradients in the SOFC solid structure and lead to large thermal stresses that can potentially result in system failure due to crack formations. In order to reduce this effect, an option is to use partial external pre-reforming, which reforms the higher hydrocarbons, possibly present in the fuel mixture, and some of the methane, reducing that way coking formation phenomena [28].

Another approach to this shortcoming is the lower temperature operation, since this would naturally reduce the endothermic MSR reaction rate. The latter is one of the reasons behind the increased research and development of intermediate temperature IR-SOFCs [32, 33].

The overall heat production from the electrochemical and water gas shift reactions is about twice the amount of heat consumed by the reforming reaction [34]. In order to regulate the temperature of the SOFC, the extra heat generated is usually removed by the flow of excess air in the cathode air channel. An example of a commercial application of the DIR-SOFC technology is the Siemens-Westinghouse SOFC prototype [35].

3 DIR-SOFC Model Description

The reforming configurations that were discussed in the previous section (IIR, DIR) can be applied to all the pro-

cesses presented (CSR, POX, ATR), but this work focuses on the study of a CSR DIR-SOFC system. The mathematical model of the processes taking place in the SOFC fuel and air channels, diffusion and reaction layers, and electrolyte is formulated by applying DGM-SMM based mass transport, the momentum conservation (Navier-Stokes equation), the energy conservation equation and the charge conservation equation, with the appropriate subdomain and boundary source terms for the chemical and electrochemical reactions. Additionally, all the corresponding boundary conditions are also determined, forming a set of coupled nonlinear PDEs that is solved within a sufficiently fine mesh, in order to produce mesh independent solutions, with the use of the finite element method (FEM) software package, COMSOL Multiphysics [36]. The model can take as input a set of design and operating physical and chemical parameters and is able to generate performance polarization curves, operating variables distributions and other measurable output parameters.

The reaction zone layers, where the anode and cathode electrochemical reactions occur at the localised TPB, causing fuel and oxidant to be converted to electrical current, heat and steam, are usually treated as mathematical boundaries. In this work, however, the electrochemically active reaction zones will be treated as finite subdomains, as can be seen in Figure 2, in order to simulate more accurately the behavior of composite electrodes, which are described next. Another unique feature of this model is that it takes into account the electrochemical oxidation of both H_2 and CO and the contribution of both reactions to the current generation.

3.1 Mixed Ionic-electronic Composite Electrodes

Mixed ionic-electronic composite electrodes have been proposed as alternatives to the simple metal cermets [37, 38]. Their use in SOFCs has many potential benefits and can
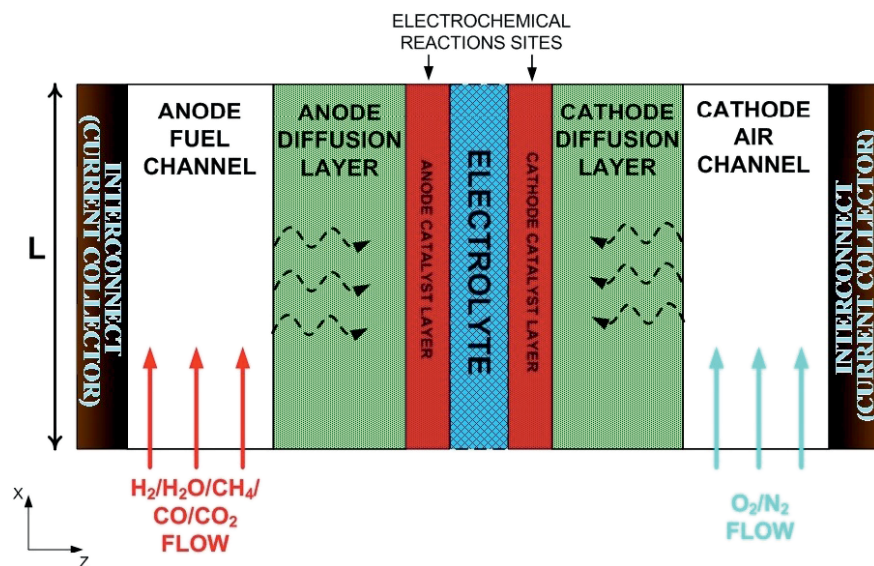

Fig. 2 Schematic of the computational domain of a cross section of a planar SOFC.

improve their performance significantly [34, 39, 40]. The composite electrodes are porous metal-loaded ceramics, which have the property of being mixed electronic and ionic conductors. The most commonly used materials for this application are Nickel/Yttria-Stabilized Zirconia (Ni/YSZ) for the anode and Lanthanum Strontium Manganate/Yttria-Stabilized Zirconia (LSM/YSZ) for the cathode.

Their primary advantage over the traditional pure electronic conducting electrodes is that the reaction zone layer for the electrochemical reaction is not limited only on the TPB, but it extends into the ceramic conductor some distance from the electrode/electrolyte interface. Subsequently, the activation overpotential losses are significantly reduced since the electrochemical reactions are better promoted [41]. Another significant advantage of composite electrodes over traditional ones is the reduction of thermal stress effects, as a result of the fact that the value of their expansion coefficient is much closer to the corresponding value of the electrolyte. This is important since the effect of the strains is mainly caused by the different thermal expansions and it is a quite common problem for SOFCs [40].

3.2 DIR-SOFC Model Kinetics

Despite the fact that catalytic steam reforming has been studied by many researchers and there are many publications providing information related to its kinetics, there are only a few dealing specifically with the reforming kinetics in SOFC anodes. In many publications [1, 11], authors claim that reforming kinetics are slow when compared with both shifting and hydrogen electrochemical oxidation, thus, under certain operating conditions, it is safe to assume that equilibrium is not reached. In the current study, for the MSR reaction (2), the following reaction rate equation will be used [10, 28]:

$$r_{MSR} = k_{MSR} p_{CH_4} \exp\left(-\frac{E^A_{MSR}}{RT}\right) \qquad (11)$$

where E^A_{MSR} is the MSR reaction activation energy and k_{MSR} is the MSR reaction pre-exponential factor.

In studies about reforming in SOFCs, several authors claim that the MSR reaction is too slow to assume that it can reach equilibrium, but on the other hand this approach is suitable for describing the kinetics of the WGS reaction [10]. Therefore, the kinetic equation that is going to be used for the WGS reaction (3) is the following [10, 28]:

$$r_{WGS} = k_{WGS} p_{CO} \left(1 - \frac{p_{CO_2} p_{H_2}/p_{CO} p_{H_2O}}{K_{eq}}\right) \qquad (12)$$

where k_{WGS} is the WGS reaction rate constant and K_{eq} is the WGS reaction equilibrium constant. The units of the reaction rates r_{MSR} and r_{WGS} given by Eqs. (12) and (13) are [mol s^{-1} m^{-2}].

The internal reforming kinetics used in this study are considered typical for Ni cermet anodes [10, 28], and they have also been used in many SOFC systems [42–46].

3.3 DIR-SOFC Model Assumptions

The main assumptions for this single cell DIR-SOFC model are gathered below:
(i)   All the water throughout the fuel channel and the porous electrode is considered to remain in the gas phase. Consequently, the model will be a single phase model and phase change as well as two phase transport will not be considered.
(ii)   The gas mixtures are assumed to behave ideally, thus the ideal gas law is applied in this model.
(iii)   The electrochemical reactions are assumed to be instantaneous and to take place at the electrochemically-active catalyst layer subdomains (see Figure 2).
(iv)   The porous electrodes are assumed to be isotropic and macro-homogeneous and the electrolyte is assumed to be impermeable to mass transport [47, 48].
(v)   The density and the heat capacity of the gas mixtures are considered constant and temperature independent throughout the SOFC.
(vi)   The thermal conductivities of the solid structures are assumed temperature independent.
(vii)   The electrical and ionic conductivities of the solid structures are described by equations that are functions of the temperature distribution.
(viii) Heat transfer due to radiation is not taken into account.
(ix)   Coke formation phenomena are not taken into consideration.
(x)   Thermal stress related phenomena are not considered in this work.

3.4 Mass, Energy, Momentum and Charge Transport Equations

The governing coupled equations and their corresponding boundary conditions of the modeling approach developed to simulate the associated mass, energy, momentum and charge conservation phenomena that occur in a DIR-SOFC will be described next. In Figure 3 the conservation principles associated with each subdomain of the computational domain are depicted.

3.4.1 Mass Transport Equations

The equation of continuity for component i, assuming an ideal gas behavior, can be written as follows [49,50]:

$$\frac{\varepsilon}{RT}\frac{\partial p_i}{\partial t} = -\nabla \cdot \mathbf{N}_i + R_i + R^{el}_i \qquad (13)$$

where ε is the porosity (equal to unity for a non-porous gas phase), $\mathbf{N}_i$ is the total molecular flux of species i, R_i and R^{el}_i are the volumetric (chemical and electrochemical, respectively) production/consumption rates of species i.

Similar to our previous work [21, 22], for the simulation of mass transport in the fuel and air channels the SMM will be employed. The multicomponent SMM is given by the following vector matrix equation for ideal gases [51]:

		Mass Transport						
---	SMM	DGM	DGM	---	DGM	DGM	SMM	---
		Momentum Transport						
---	NS	DGM	DGM	---	DGM	DGM	NS	---
		Energy Transport						
HT	HT	HT	HT	HT	HT	HT	HT	HT
		Charge Transport						
---	---	QC^{EL}	QC^{EL}	---	QC^{EL}	QC^{EL}	---	---
---	---	---	QC^{IO}	QC^{IO}	QC^{IO}	---	---	---
Anode Interconnect	Anode Fuel Channel	Anode Diffusion Layer	Anode Catalyst Layer	Electrolyte	Cathode Catalyst Layer	Cathode Diffusion Layer	Cathode Air Channel	Cathode Interconnect

Fig. 3 Schematic of the conservation equations and models used in each subdomain of the SOFC computational domain.

$$\frac{1}{RT}\nabla\mathbf{p} = \mathbf{A}^{SMM}(p_i)\mathbf{J} , i = 1, ..., n-1 \tag{14}$$

where $\mathbf{J}$ is the vector of diffusion fluxes, $\nabla\mathbf{p}$ the vector of the gradients of the partial pressures p_i and $\mathbf{A}^{SMM}(p_i)$ is a $(n-1) \times (n-1)$ matrix whose elements are given by:

$$A^{SMM}_{ii} = -\frac{p_i}{P}\left(\sum_{\substack{j=1\\j\neq i}}^{n}\frac{1}{D_{i,j}}\left(\frac{p_j}{p_i}\right) + \frac{1}{D_{i,n}}\right) \tag{15}$$

$$A^{SMM}_{ij} = \frac{p_i}{P}\left(\frac{1}{D_{i,j}} - \frac{1}{D_{i,n}}\right) \tag{16}$$

The additional equation needed in order to have a fully defined system of n equations with n unknowns is the following [51, 52]:

$$\sum_{i=1}^{n}\mathbf{J}_i = 0 \tag{17}$$

The total molecular flux $\mathbf{N}_i$ for the multidimensional SMM is given by the following equation, where the convective flux term has been added to the diffusive flux term $\mathbf{J}_i$:

$$\mathbf{N}_i = \mathbf{J}_i + c_i\mathbf{U} \tag{18}$$

where c_i is the molar concentration of species i and $\mathbf{U}$ is the velocity vector.

For the simulation of mass transport in the anode and cathode diffusion and electrochemically active catalyst layers, the DGM [53, 54] will be used taking into account the Knudsen diffusion and the Darcy's viscous flux, which is caused due to the existence of a total pressure gradient. The multidimensional DGM is given by the following vector matrix equation [50, 53, 54]:

$$\mathbf{A}^{DGM}(p_i)\mathbf{N} = \mathbf{B}^{DGM}(p_i)\nabla\mathbf{p}, \ i = 1, ..., n \tag{19}$$

where $\mathbf{N}$ and $\nabla\mathbf{p}$ are the n-dimensional vectors of component total molar fluxes and partial pressures, respectively, for all components, $\mathbf{A}^{DGM}(p_i)$ is a $n \times n$ matrix whose elements are given by:

$$A^{DGM}_{ij} = -\frac{p_i}{P\mathcal{D}_{i,j}} \tag{20}$$

$$A^{DGM}_{ii} = \sum_{\substack{j=1\\j\neq i}}^{n}\frac{p_j}{P\mathcal{D}_{i,j}} + \frac{1}{\mathcal{D}_{iK}} \tag{21}$$

$\mathbf{B}^{DGM}(p_i)$ is a $n \times n$ matrix whose elements are given by:

$$B^{DGM}_{ij} = -\frac{1}{RT}\frac{B_0 p_i}{\mathcal{D}_{iK}\mu} \tag{22}$$

$$B^{DGM}_{ii} = -\frac{1}{RT}\left(1 + \frac{B_0 p_i}{\mathcal{D}_{iK}\mu}\right) \tag{23}$$

B_0 in Eq. (22) and Eq. (23), is given by the Kozeny-Carman equation [19]:

$$B_0 = \frac{\varepsilon^3 d_P^2}{72\tau(1-\varepsilon)^2} \tag{24}$$

At the anode porous electrode the MSR and the WGS reactions are taking place. Thus, in subdomains III and IV (see Figure 4) the reaction source terms R_i used in Eq. (13) are as follows:

$$R_{H_2} = (3r_{MSR} + r_{WGS})/w_i \tag{25}$$

$$R_{H_2O} = (-r_{MSR} - r_{WGS})/w_i \tag{26}$$

$$R_{CH_4} = -r_{MSR}/w_i \tag{27}$$

$$R_{CO} = (r_{MSR} - r_{WGS})/w_i \tag{28}$$

$$R_{CO_2} = r_{WGS}/w_i \tag{29}$$

where r_{MSR} and r_{WGS} are the MSR and WGS reaction rates given by Eq. (11) and Eq. (12), and w_i is the width of each corresponding subdomain. WGS reaction is not catalytically activated and it can also be considered to take place in the fuel

channel. Thus, in subdomain II (see Figure 4) the reaction source terms R_i used in Eq. (13) are the ones described in Eqs. (25) to (29) with r_{MSR} equal to 0. In composite electrodes, the electrochemical reactions take place at the anode and cathode extended TPBs, represented here by the electrochemically-active catalyst layers (subdomains IV and VI). It has been shown that the H_2 electrochemical oxidation reaction rate is about 1.9–2.3 times and 2.3–3.1 times higher than the CO electrochemical oxidation reaction rate at 1,023 K and 1,273 K, respectively [55]. This difference is caused mainly due to the larger diffusion resistance of CO than that of H_2 in the porous electrode. Therefore, in subdomains IV and VI (see Figure 4), the electrochemical reaction source terms, R_i^{el}, of Eq. (13) are described by the following equations:

$$R_{H_2}^{el} = -\frac{I_{H_2}^A}{2F}\frac{1}{w_{ACL}} = -0.7\frac{I^A}{2F}\frac{1}{w_{ACL}} \tag{30}$$

$$R_{H_2O}^{el} = +\frac{I_{H_2}^A}{2F}\frac{1}{w_{ACL}} = +0.7\frac{I^A}{2F}\frac{1}{w_{ACL}} \tag{31}$$

$$R_{CO}^{el} = -\frac{I_{CO}^A}{2F}\frac{1}{w_{ACL}} = -0.3\frac{I^A}{2F}\frac{1}{w_{ACL}} \tag{32}$$

$$R_{CO_2}^{el} = +\frac{I_{CO}^A}{2F}\frac{1}{w_{ACL}} = +0.3\frac{I^A}{2F}\frac{1}{w_{ACL}} \tag{33}$$

$$R_{O_2}^{el} = -\frac{I^C}{4F}\frac{1}{w_{CCL}} \tag{34}$$

where I^A and I^C are the anode and cathode current densities computed by Eq. (52) and Eq. (55) presented next in this work, respectively.

Fig. 4 Schematic and numbering of the subdomains, boundaries and interfaces of the SOFC computational domain.

3.4.2 Energy Transport Equations

The energy transport equation is solved for every subdomain of the computational domain. The dominating phenomena in the current model are heat conduction, heat convection and thermal species diffusion, while energy transport by radiation is neglected. The reforming reaction is considered to take place at the anode electrode (subdomains III and IV) and the shift reaction is assumed to take place at the anode electrode (subdomains III and IV) as well as in the fuel channel (subdomain II), while the electrochemical reactions occur in the anode and cathode catalyst layers (subdomains IV and VI, respectively). The governing equation describing these phenomena is the following [51]:

$$\frac{\partial \sum_{i=1}^n c_i \bar{H}_i}{\partial t} = -\nabla \cdot \left(-k_{eff}\nabla T + \sum_{i=1}^n \bar{H}_i \mathbf{N}_i\right) + Q_h \tag{35}$$

where $\mathbf{N}_i$ is the total flux vector of species i given by Eq. (18) for the gas channels and by Eq. (19) for the porous electrodes, c_i is the molar concentration of species i, Q_h represents the thermal sources term and k_{eff} is the effective thermal conductivity given by the following expression:

$$k_{eff} = \varepsilon k_g + (1-\varepsilon)k_s \tag{36}$$

where k_g is the heat conductivity of the gas phase and k_s the heat conductivity of the solid structure. For the electrolyte and the interconnect $\varepsilon = 0$, while for the gas channels $\varepsilon = 1$. $\bar{H}_i$ is the partial molar enthalpy of species i given by the following equation [8]:

$$\bar{H}_i = \Delta \bar{H}_i^0 + \int_{T_{ref}}^T c_P^i dT \tag{37}$$

where c_P^i is the molar heat capacity of species i and $\Delta \bar{H}_i^0$ is the standard enthalpy of formation of species i.

At all the porous subdomains energy transport by convection is negligible. Accordingly, in the gas channels conductive energy transport is not taken into account. Thus, for the fuel and air channels taking into account Eq. (18), Eq. (35) takes the following form:

$$c_t c_P \frac{\partial T}{\partial t} = -c_t c_P \mathbf{U} \cdot \nabla T - \sum_{i=1}^n \mathbf{J}_i \cdot \nabla \bar{H}_i + Q_h \tag{38}$$

where c_t is the total molar concentration of the gas mixture, c_P is the molar heat capacity of the gas mixture, $\mathbf{J}_i$ is the diffusive flux vector as evaluated by the SMM in Eq. (14) and $\mathbf{U}$ is the velocity vector. The first term on the right hand side of Eq. (38) describes convection, the second one thermal species diffusion and the third one is the heat sources term.
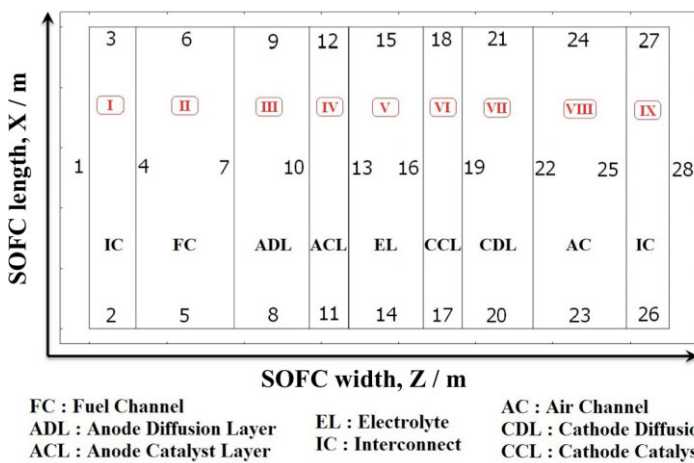
For the porous electrodes, Eq. (35) takes the following form:

$$c_t^{eff} c_P^{eff} \frac{\partial T}{\partial t} = k_{eff} \nabla^2 T - \sum_{i=1}^{n} \mathbf{N}_i \cdot \nabla \bar{H}_i + Q_h \tag{39}$$

where c_t^{eff} is the effective total molar concentration of the porous electrode and it is evaluated in the same manner as k_{eff} in Eq. (36). Similarly, c_P^{eff} is the effective molar heat capacity of the porous electrode. $\mathbf{N}_i$ is the total flux term as evaluated by the DGM in Eq. (19). In order to make these equations compatible for use with COMSOL Multiphysics, some of the terms need to make use of specific properties instead of molar. Thus, Eq. (38) and Eq. (39) were expressed as follows:

$$\rho_{eff} C_P^{eff} \frac{\partial T}{\partial t} = -\rho_{eff} C_P^{eff} \mathbf{U} \cdot \nabla T - \sum_{i=1}^{n} \mathbf{J}_i \cdot \nabla \bar{H}_i + Q_h \tag{40}$$

$$\rho_{eff} C_P^{eff} \frac{\partial T}{\partial t} = k_{eff} \nabla^2 T - \sum_{i=1}^{n} \mathbf{N}_i \cdot \nabla \bar{H}_i + Q_h \tag{41}$$

where C_P^{eff} is the effective specific heat capacity and ρ_{eff} is the effective mass density, which is evaluated by: $\rho_{eff} = \varepsilon \rho_g + (1 - \varepsilon)\rho_s$, with ρ_g being the mass density of the gas phase and ρ_s the mass density of the solid components.

At the anode and cathode diffusion and catalyst layers heat generation is taking place, due to the irreversible ohmic heating from the electronic current flow. Thus, in subdomains III, IV, VI and VII:

$$Q_h = \sigma_{el}^{eff} \nabla V_{el} \cdot \nabla V_{el} \tag{42}$$

Equivalently, at the electrolyte subdomain V, heat generation due to the resistance to the ionic current flow occurs, therefore:

$$Q_h = \sigma_{io} \nabla V_{io} \cdot \nabla V_{io} \tag{43}$$

At the anode and cathode catalyst layers the heat associated to the change of entropy due to the half-cell electrochemical reactions that cannot be utilised as electrical energy has to be taken into account. Additionally, the available energy from the open circuit voltage (OCV) that is not transformed into current, but instead is released as heat at the anode and cathode catalyst layers, has to be taken into consideration [56]. Thus, in subdomains IV and VI:

$$Q_h = \left(\frac{I_{H_2}^A}{2F} T \Delta S_{H_2}^A + \frac{I_{CO}^A}{2F} T \Delta S_{CO}^A + I^A \eta_{act}^A \right) \Big/ w_{ACL} \tag{44}$$

$$Q_h = \left(\frac{I^C}{2F} T \Delta S^C + I^C \eta_{act}^C \right) \Big/ w_{CCL} \tag{45}$$

where ΔS^A and ΔS^C are the entropy changes for each of the half-cell electrochemical reactions (4), (5) and (6) [6,7].

At the anode fuel channel, as well as at the diffusion and catalyst layers, heat associated to the MSR and WGS reactions is released. Consequently, in subdomains II, III and IV:

$$Q_h = (r_{MSR} \Delta H_{MSR} + r_{WGS} \Delta H_{WGS}) / w_i \tag{46}$$

where the reaction rates r_i and the reaction enthalpies ΔH_i are given by Eq. (11) and Eq. (12), and Eq. (2) and Eq. (3), respectively.

3.4.3 Momentum Transport Equations

The momentum transport equations are solved for the fuel and air channel subdomains II and VIII (see Figure 4). The governing equations that describe the momentum transport are the continuity and the Navier Stokes equations [36]:

$$\nabla \cdot \mathbf{U} = 0 \tag{47}$$

$$\rho \frac{\partial \mathbf{U}}{\partial t} = -(\rho \mathbf{U} \cdot \nabla)\mathbf{U} - \nabla p - \nabla \cdot \left(\eta \left(\nabla \mathbf{U} + (\nabla \mathbf{U})^T \right) \right) + \mathbf{F} \tag{48}$$

where ρ is the density of the fluid and η its kinematic viscosity.

3.4.4 Charge Transport Equations

The charge conservation equations are solved for two variables, the electronic potential V_{el} at the two electrode diffusion layers subdomains III and VII and at the two catalyst layers subdomains IV and VI, and also the ionic potential V_{io} at the electrolyte subdomain V and the two catalyst layers IV and VI (see Figure 4). The two governing equations that describe the charge conservation are the following [5, 57]:

$$\frac{\partial \rho_{el}}{\partial t} = -\nabla \cdot \left(\sigma_{el}^{eff} \nabla V_{el} \right) + Q_{el}^C \tag{49}$$

$$\frac{\partial \rho_{io}}{\partial t} = -\nabla \cdot (\sigma_{io} \nabla V_{io}) + Q_{io}^C \tag{50}$$

where ρ_{el} and ρ_{io} are the electronic and ionic charge densities respectively, σ_{el}^{eff} is the effective electronic conductivity of the electrodes, σ_{io} the ionic conductivity of the electrolyte, V_{el} and V_{io} the electronic and ionic voltages, and finally Q_{el}^C and Q_{io}^C represent the electronic and ionic charge source terms, respectively. The effective electronic conductivity of the electrodes, σ_{el}^{eff}, is given by the following expression:

$$\sigma_{el}^{eff} = \varepsilon \sigma_g + (1 - \varepsilon)\sigma_{el} \tag{51}$$

where σ_{el} is the electronic conductivity of the anode or the cathode electrode.

At the anode catalyst layer the hydrogen and carbon monoxide electrochemical oxidations are taking place and a transfer of ionic to electronic current occurs. Thus, in subdomain IV

the source terms of Eq. (49) and Eq. (50), respectively, are given by the following equations:

$$Q_{el}^C = -I^A/w_{ACL} = -I_0^A \left[\begin{array}{c} \exp\left(a^A \frac{n_eF}{RT}\eta^A\right) \\ -\exp\left(-(1-a^A)\frac{n_eF}{RT}\eta^A\right) \end{array} \right] \Big/ w_{ACL}$$

$$Q_{io}^C = I^A/w_{ACL} = I_0^A \left[\begin{array}{c} \exp\left(a^A \frac{n_eF}{RT}\eta^A\right) \\ -\exp\left(-(1-a^A)\frac{n_eF}{RT}\eta^A\right) \end{array} \right] \Big/ w_{ACL} \tag{52}$$

where w_{ACL} is the width of the anode catalyst layer (subdomain IV). The sum of the anode activation η_{act}^A and concentration overpotentials η_{conc}^A is given by [5, 58]:

$$\eta^A = \eta_{act}^A + \eta_{conc}^A = V_{el} - V_{io} \tag{53}$$

Since, in this model both the electrochemical oxidation of H_2 and CO are taken into account, the anode concentration overpotential will be computed based on the following equation:

$$\eta_{conc}^A = -\frac{RT}{n_eF} \ln\left(\frac{p_{H_2}^{bulk}p_{H_2O}^{TPB}}{p_{H_2}^{TPB}p_{H_2O}^{bulk}}\right) - \frac{RT}{n_eF} \ln\left(\frac{p_{CO}^{bulk}p_{CO_2}^{TPB}}{p_{CO}^{TPB}p_{CO_2}^{bulk}}\right) \tag{54}$$

Accordingly, at the cathode catalyst layer, where the oxygen electrochemical reduction takes place, the Butler-Volmer equation is also used to obtain the rate of transfer of electronic to ionic current. Hence:

$$Q_{el}^C = I^C/w_{CCL} = I_0^C \left[\begin{array}{c} \exp\left(a^C \frac{n_eF}{RT}\eta^C\right) \\ -\exp\left(-(1-a^C)\frac{n_eF}{RT}\eta^C\right) \end{array} \right] \Big/ w_{CCL}$$

$$Q_{io}^C = -I^C/w_{CCL} = -I_0^C \left[\begin{array}{c} \exp\left(a^C \frac{n_eF}{RT}\eta^C\right) \\ -\exp\left(-(1-a^C)\frac{n_eF}{RT}\eta^C\right) \end{array} \right] \Big/ w_{CCL} \tag{55}$$

where w_{CCL} is the width of the cathode catalyst layer (subdomain VI). Correspondingly, the sum of the cathode activation η_{act}^C and concentration overpotentials η_{conc}^C is given by [5, 58]:

$$\eta^C = \eta_{act}^C + \eta_{conc}^C = E_{REV} - (V_{el} - V_{io}) \tag{56}$$

where E_{REV} is the reversible potential also known as Nernst potential. The cathode concentration overpotential η_{conc}^C is given by: $\eta_{conc}^C = -\frac{RT}{n_eF} \ln\left(\frac{p_{O_2}^{bulk}}{p_{O_2}^{TPB}}\right)$. $I_0^{A/C}$, used in equations (52) and (55), is the exchange current density for each electrode and can be expressed as a function of the Arrhenius law and the composition of the reactant gases as:

$$I_0^A = \gamma^A \left(\frac{p_{H_2}}{p_0}\right)\left(\frac{p_{H_2O}}{p_0}\right)\exp\left(-\frac{E_A^A}{RT}\right) \tag{57}$$

$$I_0^C = \gamma^C \left(\frac{p_{O_2}}{p_0}\right)^{0.25}\exp\left(-\frac{E_A^C}{RT}\right) \tag{58}$$

where p_i is the partial pressure of the gaseous species i that takes part in an electrochemical reaction, p_0 is the reference pressure, $\gamma^{A/C}$ are the anode/cathode exchange current density pre-exponential coefficients and $E_A^{A/C}$ is the anode/cathode activation energy.

3.5 Mass, Energy, Momentum and Charge Transport Boundary Conditions

The boundary (BC) and interfacial (IFC) conditions are specified for all the external boundaries as well as the internal interfaces of the SOFC computational domain. As can be seen in Figure 4 there are in total twenty eight distinct faces, twenty of which are external boundaries and eight of which are internal interfaces. In the next sections, the BCs and IFCs for the mass, energy, momentum and charge transport equations, respectively, will be presented.

3.5.1 Mass Transport Boundary and Interfacial Conditions

At the inlet of the fuel and air channels, the partial pressures p_i of each species i are specified. Therefore, according to Figure 4:

$$BC5 : p_i = p_i^{IN} , i = H_2, H_2O, CH_4, CO, CO_2 \tag{59}$$

$$BC23 : p_i = p_i^{IN} , i = O_2, N_2 \tag{60}$$

where p_i^{IN} is the partial pressure of species i at the inlet.

At the outlet of the fuel and air channels convective flux boundary conditions are imposed, meaning that the diffusive term of the total flux is cancelled out and only the convective term is taken into account. Thus:

$$BC6 : J_i^{FC} = 0 , i = H_2, H_2O, CH_4, CO, CO_2 \tag{61}$$

$$BC24 : J_i^{AC} = 0 , i = O_2, N_2 \tag{62}$$

where J_i^{FC} and J_i^{AC} are the diffusive fluxes of species i at the fuel and air channels, respectively.

At the fuel channel/anode diffusion layer interface and at the air channel/cathode diffusion layer interface, continuity for the partial pressure and for the flux terms of each species i is imposed. Therefore:

$$IFC7 : p_i^{FC} = p_i^{ADL} \ \& \ N_i^{FC} = N_i^{ADL}, \ i = H_2, H_2O, CH_4, CO, CO_2 \tag{63}$$

$$IFC22 : p_i^{AC} = p_i^{CDL} \ \& \ N_i^{AC} = N_i^{CDL}, \ i = O_2, N_2 \tag{64}$$

where p_i^{FC} and p_i^{AC}, p_i^{ADL} and p_i^{CDL} are the partial pressures of species i at the fuel and air channels, and at the anode and cathode diffusion layers, respectively. Correspondingly, N_i^{FC} and N_i^{AC}, N_i^{ADL} and N_i^{CDL} are the total molar fluxes of species i at the fuel and air channels, and at the anode and cathode diffusion layers, respectively.

Similarly, at the anode diffusion layer/anode catalyst layer interface and at the cathode diffusion layer/cathode catalyst layer interface, continuity for the partial pressure and for the flux terms of each species i is imposed. Therefore:

$$IFC10 : p_i^{ADL} = p_i^{ACL} \ \& \ N_i^{ADL} = N_i^{ACL},$$
$$i = H_2, H_2O, CH_4, CO, CO_2 \tag{65}$$

$$IFC19 : p_i^{CDL} = p_i^{CCL} \ \& \ N_i^{CDL} = N_i^{CCL}, \ i = O_2, N_2 \tag{66}$$

where p_i^{ACL} and p_i^{CCL} are the partial pressures of species i at the anode and cathode catalyst layers, respectively. Correspondingly, N_i^{ACL} and N_i^{CCL} are the total molar fluxes of species i at the anode and cathode catalyst layers, respectively.

At all the remaining boundaries and interfaces, insulation BCs are imposed.

3.5.2 Energy Transport Boundary and Interfacial Conditions

At the inlet of the fuel and air channels the temperature T of each gas stream is specified. Therefore:

$$BC5 : T_{II} = T_{IN}^{FC} \tag{67}$$

$$BC23 : T_{VIII} = T_{IN}^{AC} \tag{68}$$

Similar to mass transport, at the outlet of the fuel and air channels convective flux boundary conditions for the energy transport are imposed, which means that the conductive term of the total flux is cancelled out and only the convective term is taken into account. Thus:

$$BC6 : -\mathbf{n} \cdot (-k_{II} \nabla T_{II}) = 0 \tag{69}$$

$$BC24 : -\mathbf{n} \cdot (-k_{VIII} \nabla T_{VIII}) = 0 \tag{70}$$

where k_j is the thermal conductivity of subdomain j and $\mathbf{n}$ is the unit normal vector pointing outwards relative to the subdomains.

At the fuel channel/anode electrode interface and at the air channel/cathode electrode interface, convective heat flux boundary conditions are imposed. Thus, according to Figure 4:

$$IFC7 : -\mathbf{n} \cdot (-k_{III} \nabla T_{III}) = h_{FC/ADL}(T_{II} - T_{III}) \tag{71}$$

$$IFC22 : -\mathbf{n} \cdot (-k_{VII} \nabla T_{VII}) = h_{AC/CDL}(T_{VIII} - T_{VII}) \tag{72}$$

where h_k is the convective heat transfer coefficient at interface k.

At the fuel channel/interconnect interface and at the air channel/interconnect interface, convective heat flux boundary conditions are imposed. Therefore:

$$IFC4 : -\mathbf{n} \cdot (-k_I \nabla T_I) = h_{FC/AIC}(T_{II} - T_I) \tag{73}$$

$$IFC25 : -\mathbf{n} \cdot (-k_{IX} \nabla T_{IX}) = h_{AC/CIC}(T_{VIII} - T_{IX}) \tag{74}$$

At the anode diffusion layer/catalyst layer and at the cathode diffusion layer/catalyst layer interfaces, temperature continuity conditions are considered. Hence:

$$IFC10 : T_{III} = T_{IV} \ \& \ -\mathbf{n}_u \cdot (-k_{III} \nabla T_{III}) - \mathbf{n}_d \cdot (-k_{IV} \nabla T_{IV}) = 0 \tag{75}$$

$$IFC19 : T_{VI} = T_{VII} \ \& \ -\mathbf{n}_u \cdot (-k_{VI} \nabla T_{VI}) - \mathbf{n}_d \cdot (-k_{VII} \nabla T_{VII}) = 0 \tag{76}$$

where $\mathbf{n}_u$ and $\mathbf{n}_d$ are the unit normal vectors pointing outwards relative to the subdomains.

Accordingly, at the anode catalyst layer/electrolyte and at the cathode catalyst layer/electrolyte interfaces, temperature continuity conditions are applied. Hence:

$$IFC13 : T_{IV} = T_V \ \& \ -\mathbf{n}_u \cdot (-k_{IV} \nabla T_{IV}) - \mathbf{n}_d \cdot (-k_V \nabla T_V) = 0 \tag{77}$$

$$IFC16 : T_V = T_{VI} \ \& \ -\mathbf{n}_u \cdot (-k_V \nabla T_V) - \mathbf{n}_d \cdot (-k_{VI} \nabla T_{VI}) = 0 \tag{78}$$

At the end of each of the two interconnect subdomains, symmetry boundary conditions are imposed, assuming that the cell is placed in the middle of a SOFC stack. In order to achieve this, the feature of extrusion coupling variables [36] incorporated in COMSOL Multiphysics was used. Therefore, according to Figure 4:

$$IFC1 : T_I = T_{IX} \tag{79}$$

$$IFC28 : -\mathbf{n} \cdot (-k_I \nabla T_I) = -\mathbf{n} \cdot (-k_{IX} \nabla T_{IX}) \tag{80}$$

At all the remaining boundaries insulation BCs are imposed.

3.5.3 Momentum Transport Boundary and Interfacial Conditions

At the inlet of the fuel and air channels the velocity $\mathbf{U}$ of each gas stream is specified. Therefore:

$$BC5 : \mathbf{U}_{II} = \mathbf{U}_{IN}^{FC} \tag{81}$$

$$BC23 : \mathbf{U}_{VIII} = \mathbf{U}_{IN}^{AC} \tag{82}$$

At the outlet of the fuel and air channel pressure boundary conditions are imposed, which are typical for this type of problem. Thus:

$$BC6 : p_{II} = p^A \tag{83}$$

$$BC24 : p_{VIII} = p^C \tag{84}$$

At all the remaining boundaries no slip BCs are imposed.

3.5.4 Charge Transport Boundary and Interfacial Conditions

At the fuel channel/anode diffusion layer interface, the electronic voltage, V_{el}, is arbitrarily set to zero [47, 59, 60]. Therefore:

$$IFC7 : V_{el} = 0 \tag{85}$$

At the air channel/cathode diffusion layer interface, the electronic voltage, V_{el}, is set equal to the operating voltage V_C of the SOFC [47, 59, 60]. Thus:

$$IFC22 : V_{el} = V_C \tag{86}$$

At the anode diffusion layer/catalyst layer and at the cathode diffusion layer/catalyst layer interfaces, electronic voltage, V_{el}, continuity conditions are applied. Thus:

$$IFC10 : -\mathbf{n} \cdot \left(\sigma_{el}^{eff} \nabla V_{el}^{III} - \sigma_{el}^{eff} \nabla V_{el}^{IV} \right) = 0 \tag{87}$$

$$IFC19 : -\mathbf{n} \cdot \left(\sigma_{el}^{eff} \nabla V_{el}^{VI} - \sigma_{el}^{eff} \nabla V_{el}^{VII} \right) = 0 \tag{88}$$

Accordingly, at the anode catalyst layer/electrolyte and at the cathode catalyst layer/electrolyte interfaces, ionic voltage, V_{io}, continuity conditions are applied. Hence:

$$IFC13 : -\mathbf{n} \cdot \left(\sigma_{io}^{eff} \nabla V_{io}^{IV} - \sigma_{io}^{eff} \nabla V_{io}^{V} \right) = 0 \tag{89}$$

$$IFC16 : -\mathbf{n} \cdot \left(\sigma_{io}^{eff} \nabla V_{io}^{V} - \sigma_{io}^{eff} \nabla V_{io}^{VI} \right) = 0 \tag{90}$$

At all the remaining boundaries and interfaces, insulation BCs are imposed.

4 Results and Discussion

The DIR-SOFC model developed here is based on fundamental equations written in a partial differential form, making it flexible in terms of the geometries that can be used. Thus, planar, tubular and monolithic DIR-SOFC configurations can

be simulated using this model, provided that the corresponding BCs are modified accordingly. The computational domain was discretized in 29,021 domain and 3,473 boundary triangular elements, which were sufficient to produce mesh-independent solutions. In the current model the operating voltage V_C is considered constant throughout the SOFC, therefore it will be a degree of freedom for the model. On the other hand, the current density I_C is considered a dependent variable, thus it will vary throughout the solid structure of the SOFC. The pre-exponential coefficients, activation energies and equilibrium constants, used in the MSR and WGS reactions rate Eqs. (11) and (12), depend on the physical and chemical properties of the DIR-SOFC materials. In this work data from the literature have been used. In Table 1 the DIR-SOFC model parameters

Table 1 DIR-SOFC model energy and charge transport parameters.

Parameter / Units	Symbol	Value
Anode electrode thermal conductivity / W m^{-1}K^{-1}	k_s^A	10 [61]
Fuel mixture thermal conductivity / W m^{-1}K^{-1}	k_g^A	0.32 [62]
Cathode electrode thermal conductivity / W m^{-1}K^{-1}	k_s^C	11 [61]
Air mixture thermal conductivity / W m^{-1}K^{-1}	k_g^C	0.58 [62]
Electrolyte thermal conductivity / W m^{-1}K^{-1}	k_E	2 [61]
Interconnects thermal conductivity / W m^{-1}K^{-1}	k_{IC}	6 [61]
Anode specific heat capacity / J kg^{-1}K^{-1}	C_p^A	0.65 [63]
Cathode specific heat capacity / J kg^{-1}K^{-1}	C_p^C	0.9 [63]
Electrolyte specific heat capacity / J kg^{-1}K^{-1}	C_p^E	0.3 [63]
Interconnects specific heat capacity / J kg^{-1}K^{-1}	C_p^{IC}	0.8 [63]
Anode electrode density / kg m^{-3}	ρ_s^A	6,200 [63]
Cathode electrode density / kg m^{-3}	ρ_s^C	6,000 [63]
Electrolyte density / kg m^{-3}	ρ_s^E	5,560 [63]
Interconnects density / kg m^{-3}	ρ_s^{IC}	7,700 [63]
Convective heat transfer coefficient / W m^{-2}K^{-1}	h_i	5 [64]
Anode electrode electrical conductivity / Ω^{-1} m^{-1}	σ_{ADL}^{el}	$\frac{9.5 \times 10^7}{T} \exp\left(-\frac{1150}{T}\right)$ [65]
Cathode electrode electrical conductivity / Ω^{-1} m^{-1}	σ_{CDL}^{el}	$\frac{4.2 \times 10^7}{T} \exp\left(-\frac{1200}{T}\right)$ [65]
Electrolyte ionic conductivity / Ω^{-1} m^{-1}	σ_E^{io}	$33400 \exp\left(-\frac{10300}{T}\right)$ [65]
Anode transfer coefficient / –	a^A	0.5
Cathode transfer coefficient / –	a^C	0.5
Anode pre-exponential coefficient / A m^{-2}	γ^A	7.55×10^9 [66]
Cathode pre-exponential coefficient / A m^{-2}	γ^C	6.91×10^8 [66]
Anode activation energy / J gmol^{-1}	E_A^A	120,000 [66]
Cathode activation energy / J gmol^{-1}	E_A^C	110,000 [66]

are listed along with the corresponding sources, they were extracted from. In order to study the effect of different operating and design parameters on the SOFC performance, base case parameters have to be defined. The base case operating and design parameters used in this model, considering steady-state conditions, are listed in Table 2.

The binary diffusion coefficients of the species used are temperature and pressure dependent and they are calculated using the Fuller's method [68]:

$$D_{A,B} = \frac{0.00143 T^{1.75}}{P M_{AB}^{1/2} \left[(\Sigma_v)_A^{1/3} + (\Sigma_v)_B^{1/3} \right]^2} \tag{91}$$

The Knudsen diffusion coefficients of the participating species i are calculated by[69]:

$$D_{iK} = \frac{4}{3} K_0 \sqrt{\frac{8RT}{\pi M_i}} \tag{92}$$

4.1 Model Validation

Our model has been validated against experimental data available in literature [70]. The geometrical aspects of the experimental setup have been reported in [71]. The geometry of the model defined in Tables 1 and 2 has been adapted to match the experimental one. Table 3 outlines the geometrical aspects of the model used for the validation, as well as the material parameters, as reported in [71]. All parameters not mentioned in Table 3, have the same value as in the base case (Tables 1 and 2). The feed reported in [71] is 1.66×10^{-3} l s^{-1},

Table 2 Base case operating conditions and kinetic parameters for the DIR-SOFC model.

Parameter / Units	Symbol	Value
Fuel inlet temperature / K	T_{IN}^A	1,173
Air inlet temperature / K	T_{IN}^C	1,173
Fuel channel inlet velocity / m s^{-1}	$\mathbf{U}_{IN}^{FC}$	0.2
Air channel inlet velocity / m s^{-1}	$\mathbf{U}_{IN}^{AC}$	5.0
Operating pressure / atm	P	1
Gas law constant / m^3 atm gmol^{-1} K^{-1}	R	8.20575×10^{-5}
Viscosity / N s m^{-2}	μ	2.01×10^{-5}
Permeability / m^2	B_0	1.98×10^{-10}
Faraday's constant / A s gmol^{-1}	F	96485.3
Porosity / –	ε	0.46
Tortuosity / –	τ	4.5
Average pore radius / m	$\bar{r}$	2.6×10^{-6}
Fuel cell length / m	L	0.05
Fuel channel width / m	w_{FC}	0.0022
Air channel width / m	w_{AC}	0.0022
Anode diffusion layer width / m	w_{ADL}	0.0004
Cathode diffusion layer width / m	w_{CDL}	0.00015
Anode catalyst layer width / m	w_{ACL}	0.0001
Cathode catalyst layer width / m	w_{CCL}	0.00005
Electrolyte width / m	w_E	0.0003
Anode interconnect width / m	w_{AIC}	0.001
Cathode interconnect width / m	w_{CIC}	0.001
Operating Voltage / V	V_C	0.6
MSR reaction activation energy / J mol^{-1}	E_{MSR}^A	82,000 [10]
MSR reaction pre-exponential constant / mol s^{-1} m^{-2} atm^{-1}	k_{MSR}	4,331 [10]
WGS reaction equilibrium constant / –	K_{eq}	1.44 [67]
WGS reaction pre-exponential factor / mol s^{-1} m^{-2} atm^{-1}	k_{WGS}	101.325 [67]

Table 3 Parameters for the DIR-SOFC model used for model validation [71].

Parameter / Units	Symbol	Value
Fuel inlet temperature / K	T_{IN}^A	1,073
Air inlet temperature / K	T_{IN}^C	1,073
Fuel channel inlet velocity / m s^{-1}	$\mathbf{U}_{IN}^{FC}$	0.171
Air channel inlet velocity / m s^{-1}	$\mathbf{U}_{IN}^{AC}$	0.171
Operating pressure / atm	P	1
Gas law constant / m^3 atm gmol^{-1} K^{-1}	R	8.20575×10^{-5}
Viscosity / N s m^{-2}	μ	2.01×10^{-5}
Permeability / m^2	B_0	1.98×10^{-10}
Porosity / –	ε	0.35
Tortuosity / –	τ	3.8
Fuel channel width / m	w_{FC}	0.0022
Air channel width / m	w_{AC}	0.0022
Anode diffusion layer width / μm	w_{ADL}	400
Cathode diffusion layer width / μm	w_{CDL}	15
Anode catalyst layer width / μm	w_{ACL}	100
Cathode catalyst layer width / μm	w_{CCL}	15
Electrolyte width / μm	w_E	25
Anode electrode thermal conductivity / W m^{-1}K^{-1}	k_s^A	3
Cathode electrode thermal conductivity / W m^{-1}K^{-1}	k_s^C	3.8
Electrolyte thermal conductivity / W m^{-1}K^{-1}	k_E	1.8
Anode convective heat transfer coefficient / W m^{-2}K^{-1}	h_A	57
Cathode convective heat transfer coefficient / W m^{-2}K^{-1}	h_C	49
Anode pre-exponential coefficient / A m^{-2}	γ^A	1.344×10^{10} [72]
Cathode pre-exponential coefficient / A m^{-2}	γ^C	2.051×10^{9} [72]
Anode activation energy / J gmol^{-1}	E_A^A	120,000 [72]
Cathode activation energy / J gmol^{-1}	E_A^C	100,000 [72]

which corresponds to a maximum velocity at the fuel channel of 0.171 m s^{-1} if a parabolic velocity profile is assumed. The reversible voltage has been adapted from experimental data (1.17 V), since the empirical relation used for our model is incompatible with the experimental data utilized. The pre-exponential coefficient and the activation energy for the exchange current density used in the modified Butler-Volmer equation were obtained from [72]. The fuel mixture used for the model validation is 30% pre-reformed and it consists of 26.3% H_2, 49.3% H_2O, 17.1% CH_4, 2.9% CO and 4.4% CO_2 at the inlet to the fuel channel [71].

The polarization curve obtained using our model is compared to the experimental results and it is illustrated in Figure 5. The model is shown to replicate the experiment sufficiently well. Small discrepancies are attributed to some geometrical aspects being unavailable and to some of the literature-obtained parameter referring to different conditions and materials than the ones used in the actual experimental setup.

4.2 Base Case Model Simulations

Our DIR-SOFC system is designed to operate for both non pre-reformed and pre-reformed operating conditions. The fuel mixture used in this study is 10 % pre-reformed and it consists of 8% H_2, 58% H_2O, 28% CH_4, 2% CO and 4% CO_2 at the inlet of the fuel channel [10].

In Figure 6, the H_2 and O_2 molar fractions at the anode fuel channel and at the cathode air channel are illustrated. As H_2 and O_2 flow in the fuel and air channels, respectively, they diffuse through the porous electrodes where they react at the anode and cathode electrochemically-active catalyst layers respectively, where the half-cell electrochemical oxidation (4) and reduction (6) reactions take place. In the porous electrodes, the formed gradients of the H_2 and O_2 molar fractions are larger than in the fuel and air channel, because the diffusion is more difficult in the porous electrodes than in the fuel and air channels. Additionally, at the fuel and air channels the convective effects are much larger compared to the porous

electrodes, where diffusion prevails. Close to the inlet of the fuel channel, a steep increase of the H_2 partial pressure can be observed. This is due to the rapid MSR reaction (2) and is an indication that this occurs mainly close to the fuel inlet. After all CH_4 is depleted, the produced H_2 is then gradually consumed along the length of the cell by the electrochemical reaction (4), resulting in the decrease of its molar fraction after reaching a maximum value. The O_2 molar fraction at the cathode electrochemically active catalyst layer is decreased along the length of the air channel due to the half-cell electrochemical reduction reaction, as expected.

Figure 7 illustrates the anode fuel gas species molar fractions along the length of the fuel channel. The impact of the simultaneous occurrence of the MSR reaction, the WGS reaction and the electrochemical oxidation of H_2 and CO at the anode catalyst layer is presented. A rapid decrease in the CH_4 composition and a corresponding increase in the H_2 composition can be seen close to the inlet of the fuel channel. This is due to the very fast MSR reaction (2) and partially because of the WGS reaction. A decrease in the H_2O composition can also be observed, which can also be attributed to the MSR and WGS reactions as steam plays the role of the reactant in these reactions. However, H_2 and H_2O are also participating in the H_2 electrochemical reaction (4), where they have an opposite role, although the effect of the MSR and WGS reactions cannot be balanced, due to the different reaction rates. When CH_4 starts getting depleted, H_2 and H_2O compositions begin to decrease and increase respectively, as now the effect of the electrochemical reactions is dominating. Consequently, the H_2 and H_2O compositions exhibit a maximum and a minimum respectively, close to the point where CH_4 is depleted. Similarly to H_2, at the inlet region there is an increase in CO composition due to the MSR reaction, which starts decreasing as soon as CH_4 is consumed and the WGS and the CO electrochemical reactions dominate. These trends, presented in Figure 7, come in qualitative agreement with results from [10] and [19], but vary quantitatively due to the use of different operating parameters.

In Figure 8, the temperature distribution in the DIR-SOFC, obtained by the developed model, is illustrated. Inlet temperatures of $T_{IN}^A = T_{IN}^C = 1,173$ K and base case conditions, as given in Table 2, were used for this simulation. The steep temperature decrease, that results in a cold spot at the anode electrode near the fuel inlet, is a result of the excessive amount of heat consumed by the highly endothermic MSR reaction (2). The DIR-SOFC temperature decreases in the first 20% of its length by 50 K in relation to its inlet value. CH_4 is depleted near the inlet due to the large MSR reaction (2) rate and as a result, the exothermic electrochemical reactions (4) and (5) dominate the thermal energy generation, leading to a temperature increase all the way to the exit of the fuel and air channels. This causes the formation of thermal gradients that in turn give rise to thermal stresses, as already discussed. If these stres-
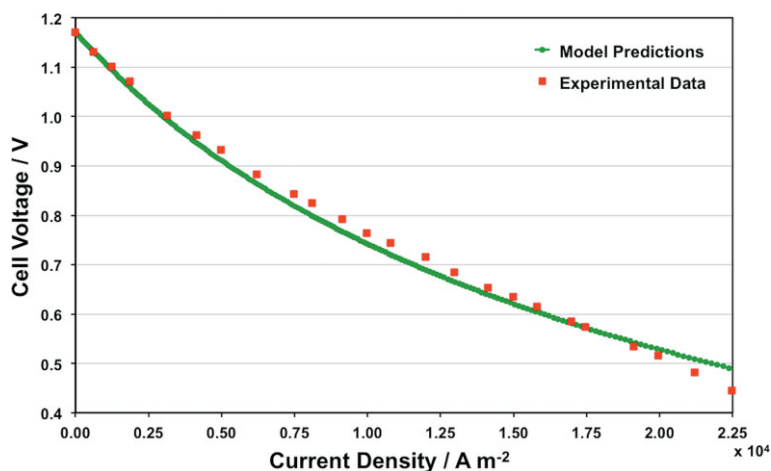

Fig. 5 Polarization curve computed by the proposed model against experimental results [70].
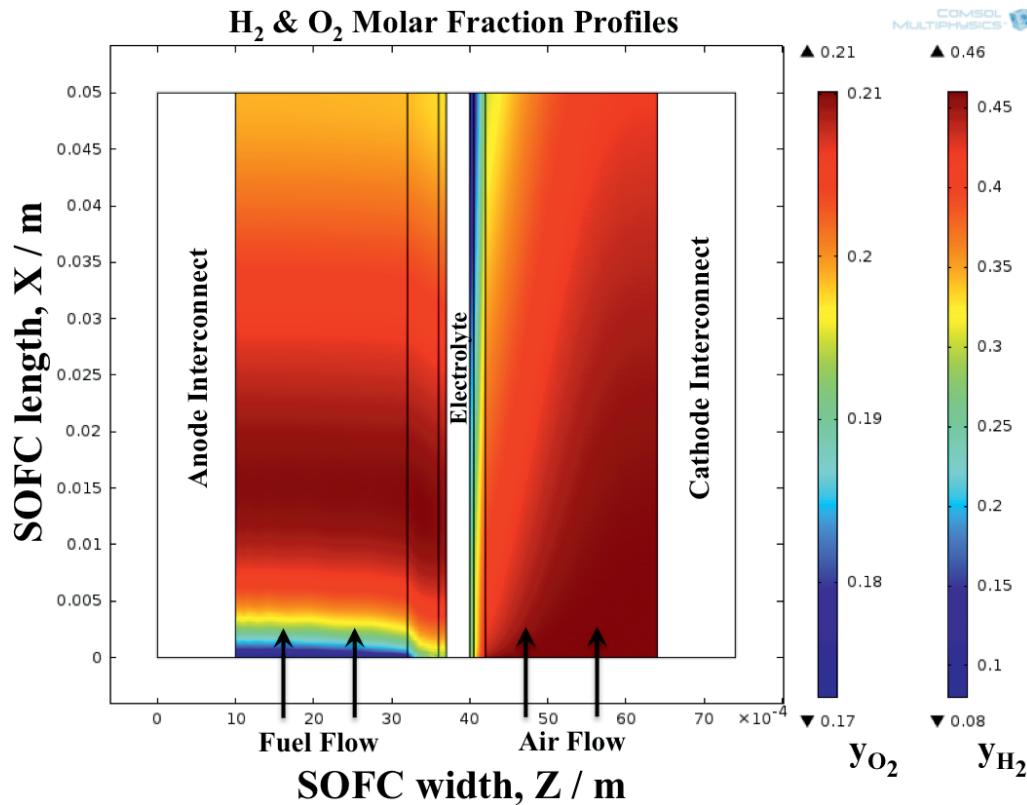
Fig. 6 H_2/O_2 molar fraction profiles at the anode/cathode side of the DIR-SOFC for base case inlet compositions.
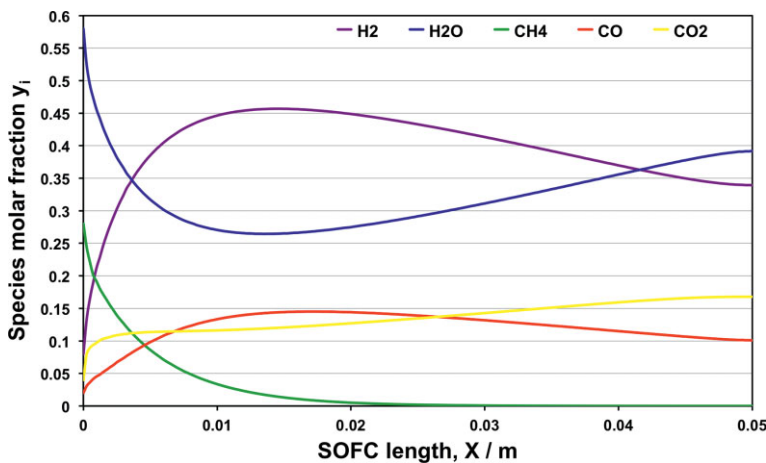

Fig. 7 Fuel species molar fractions y_i distribution along the length of the SOFC for base case inlet compositions.

ses exceed the threshold values dictated by the ceramic and metal materials used for the construction of the SOFC, it can result in reduced performance and even mechanical failure of the cell.

Figure 9 illustrates the average (along the SOFC length) electronic and ionic voltage distributions along both diffusion and catalyst layers and the electrolyte domain for base case conditions (as in Table 2) and for operating potential $V_C =$ 0.6 V. As mentioned previously, since electrons cannot flow in the electrolyte and ions cannot flow through the diffusion

layers of the electrodes, there is no electronic and ionic potential at the respective subdomains. The current densities are defined by the gradient of the respective ionic and electronic voltage curves in Figure 9. The activation and concentration overpotentials are given by Eq. (53) and Eq. (56) respectively and as can be seen for the selected operating conditions the anode overpotential is slightly larger than the cathode one. The ohmic overpotential is almost zero at the electrodes as their electronic conductivity is much higher compared to the electrolyte ionic conductivity. The ionic potential distribution in the electrolyte subdomain is linear due to the constant ionic current flux.

The average current density and the reversible voltage distributions along the length of the cell are shown in Figure 10. The current density decreases to a minimum of 6,200 A m^{-2} and then increases along the length of the cell. Its magnitude is dependent on the temperature and on the H_2 and CO concentrations. The temperature dependence is more significant, as it is evident from the trend observed in Figure 11, which agrees with the temperature decrease close to the inlet of the DIR-SOFC. Accordingly, the reversible voltage E_{REV} exhibits a peak value at the point where the temperature is at its lowest value as expected from the expression:
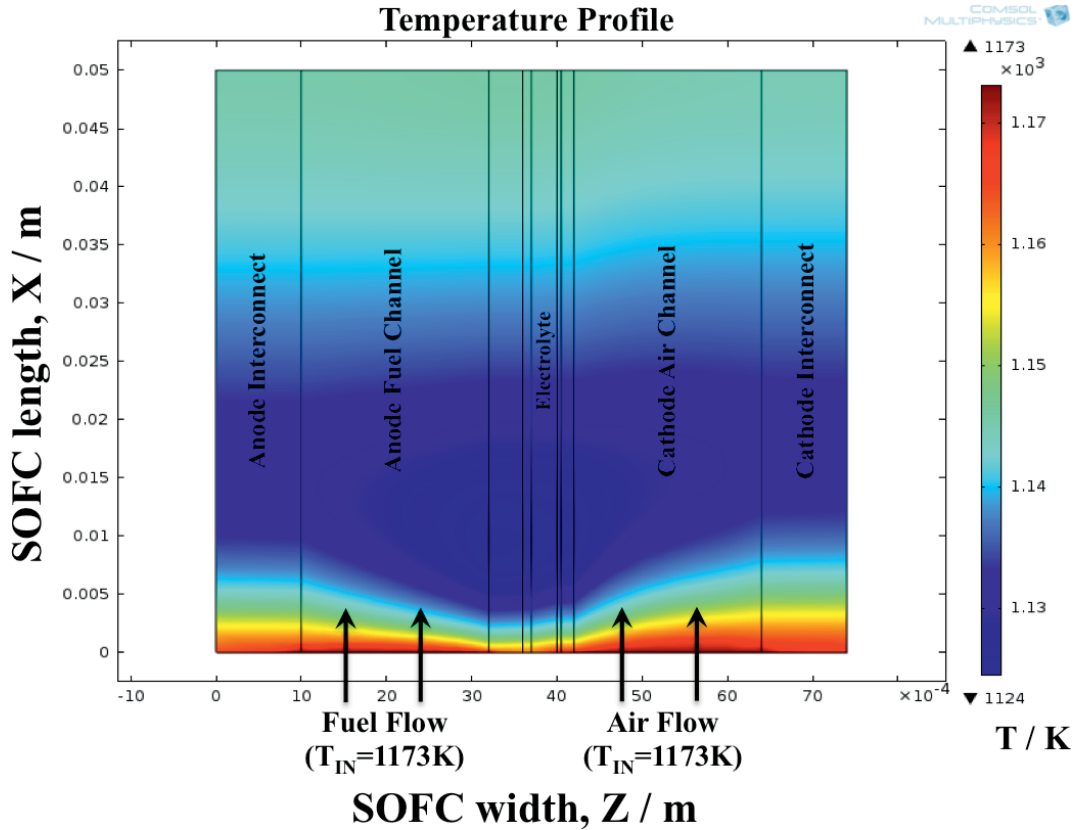
Fig. 8   Temperature profile in the DIR-SOFC domain (MSR reaction endothermic effect).
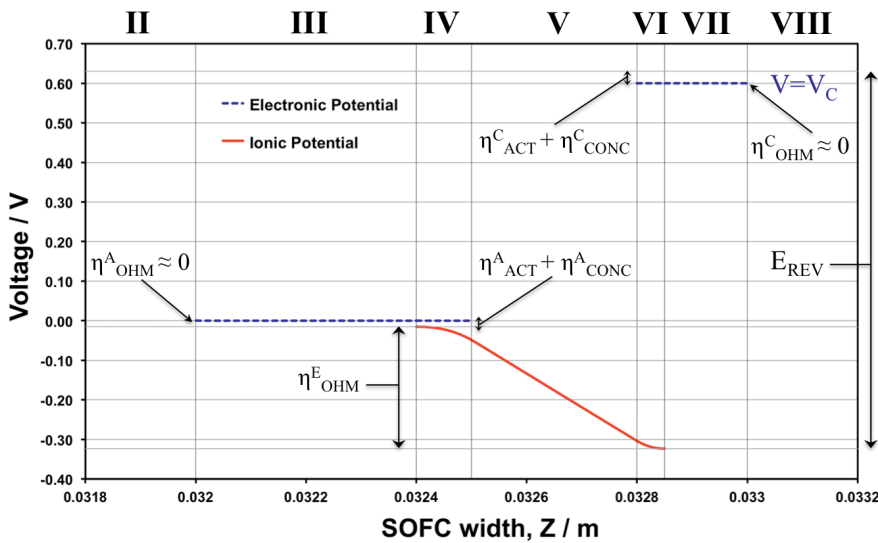

Fig. 9   Average (along the length) electronic and ionic voltage distributions over the width of the solid DIR-SOFC domains for base case operating conditions.

$$E_{REV} = E_0 + \frac{RT}{n_e F} \ln\left(\frac{p_{H_2} p_{O_2}^{0.5}}{p_{H_2O}}\right) \qquad (93)$$

4.3 Parametric Investigation

A parametric study of various operating and design parameters has been performed in order to examine their effect on the performance of the DIR-SOFC. In Figure 11, temperature distributions along the length of the SOFC, for fuel and air channel inlet temperatures of 1,073 K, 1,123 K, and 1,173 K and for a constant operating voltage $V_C = 0.6$ V, are depicted. As discussed previously, the temperature exhibits a minimum close to the inlet of the fuel channel, where the rate of the endothermic MSR reaction (2) reaches its highest value. It can be seen that the temperature gradient is smoother for inlet temperature $T_{IN} = 1,073$ K than for $T_{IN} = 1,173$ K. This can be attributed mainly to the fact that, for constant V_C, higher temperature operation corresponds to higher average current densities, resulting in higher exothermic electrochemical oxidation reaction rates and in turn in a more steep increase of the temperature along the cell. Furthermore, the MSR reaction rate increases with increasing temperature, as expected from Eq. (11), which also affects the formation of larger gradients.
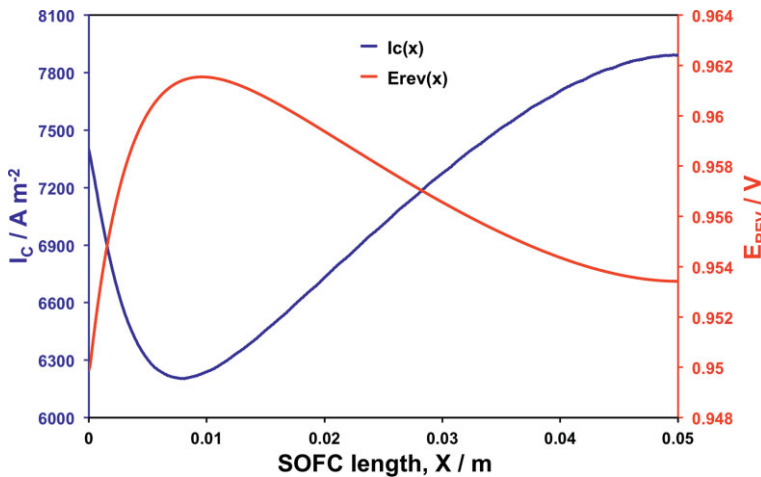
Fig. 10 Average (along the catalyst layer width) current density and reversible voltage distribution along the cathode catalyst layer length of the DIR-SOFC.

In Figure 12, temperature distributions along the length of the SOFC, for fuel and air channel inlet temperatures of 1,073 K, 1,123 K, and 1,173 K and for constant average current density I_C = 7,100 A m^{-2}, are depicted. It is observed that for lower inlet temperatures the temperature profile is slightly smoother (green line) than the corresponding one for higher inlet temperatures (blue line). This can be explained by the lower endothermic MSR reaction rate exhibited at lower temperatures, which is the only significant factor in this case, in contrast to the previous case where the change in the current density can also affect the temperature profile.

Figure 13 illustrates the predicted average current density and power density as functions of the operating voltage, for fuel and air channel inlet temperatures of 1,073 K, 1,123 K, and 1,173 K and for the base case operating conditions as listed in Table 2. As can be seen in Figure 13, the power output of the DIR-SOFC, which is given by the operating voltage
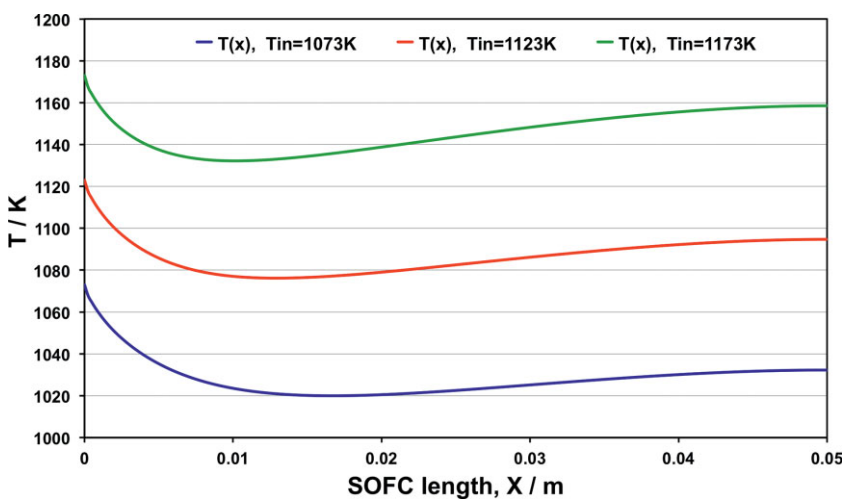
multiplied by the average current density, increases with rising temperature, as expected since the cell's overpotentials decrease. Therefore, the operating voltage is higher for the same current density. The decrease in the cell's overpotentials is caused by the decrease of each individual overpotential term. The ohmic overpotential decreases with increasing temperature, because the ionic and electronic conductivities increase accordingly, as can be seen from their equations in Table 1. The activation overpotential is also decreasing with increasing temperature, since the activity of the electrochemical reactions increases at higher temperatures. This can also be deduced from the current density and the exchange current density expressions (Eqs. (52), (55), (57), and (58)), where under typical SOFC operating conditions, a temperature increase leads to a decrease in the activation overpotential, since the exchange current density is an increasing function of temperature. Finally, at higher temperatures the diffusivity of the species is increased, resulting in lower values of concentration overpotentials, as the species can diffuse easier through the porous diffusion layer. Furthermore, in a DIR-SOFC the reaction rates of the MSR and WGS reactions are enhanced with increasing temperature, resulting in higher H_2 and CO concentrations and subsequently in higher current densities. Higher operating temperatures also result in lower reversible voltages, as expected by Eq. (93), but also in higher limiting current density values.

In Figure 14, polarization and power density curves for anode catalyst layer thicknesses of 0.0002 m, 0.0001 m and 0.00005 m and for the base case operating conditions (as in Table 2), are depicted. For this parametric investigation, the total thickness of the anode electrode, *i.e.* the diffusion and the catalyst layer, was kept constant. Increasing the electrochemically-active catalyst layer thickness results in an increased total rate of the electrochemical reactions and, consequently, in reduced activation overpotential [73]. However, the ionic ohmic overpotential is increased, since the distance the ions have to travel to reach the reaction sites increases. For the operating conditions and design parameters used in this case, the increase in the ohmic overpotential is more significant than the decrease in the activation overpotential, therefore, a slight decrease in the DIR-SOFC performance is observed for higher values of the anode catalyst layer thickness.

5 Conclusions

The development and use of a comprehensive, 2-dimensional, multicomponent, non-isothermal, dynamic model for the investiga-
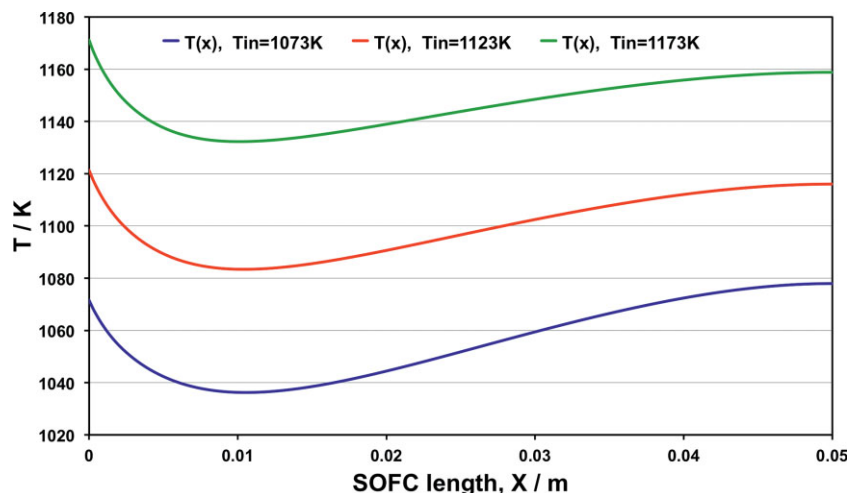

Fig. 11 Temperature distribution along the length of the SOFC for constant operating voltage V_C = 0.6 V at a range of fuel and air channel inlet temperatures T_{IN}^A and T_{IN}^C (1,173 K – 1,123K – 1,073K).

Fig. 12 Temperature distribution along the length of the SOFC for constant average current density I_C = 7,100 A m^{-2} at a range of fuel and air channel inlet temperatures T_{IN}^A and T_{IN}^C (1,173 K – 1,123 K – 1,073 K).
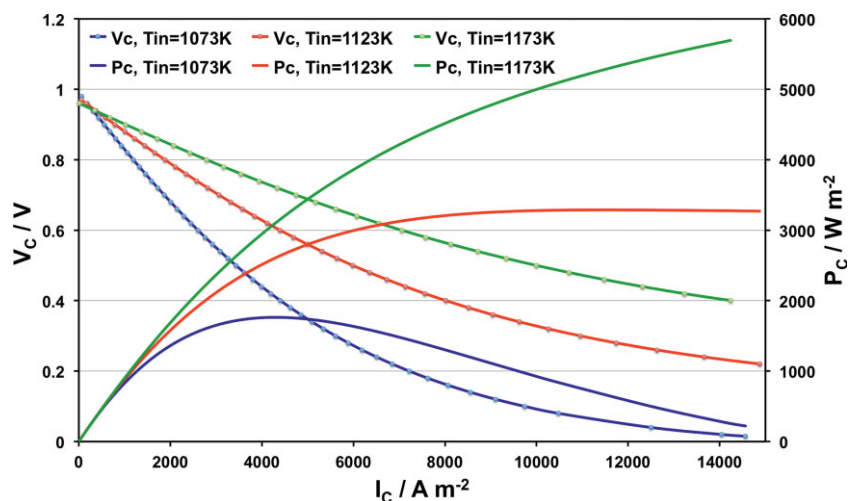

Fig. 13 Operating voltage V_C and power density P_C as functions of the average current density I_C at a range of fuel and air channel inlet temperatures T_{IN}^A and T_{IN}^C (1,173 K – 1,123 K – 1,073 K).
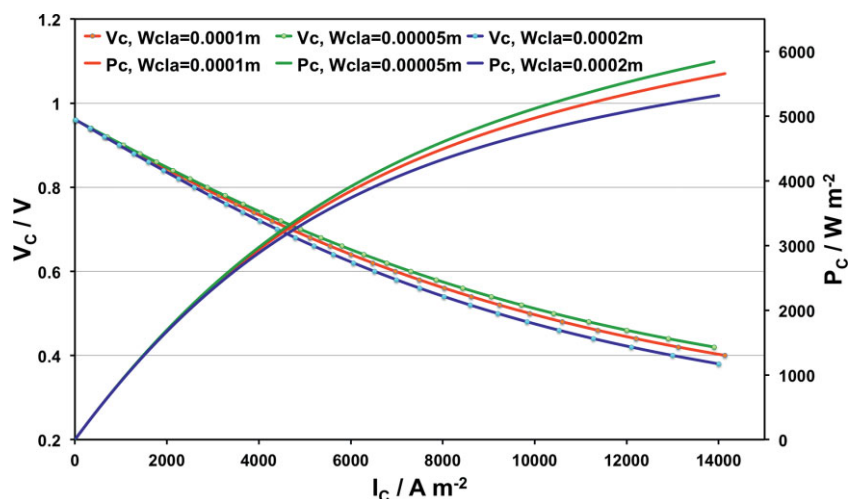

Fig. 14 Operating voltage V_C and power density P_C as functions of the average current density I_C for different anode catalyst layer widths w_{ACL} (0.00005 m – 0.0001 m – 0.0002 m).

tion of the thermal and electrochemical phenomena in a planar DIR-SOFC, that utilises a mixture of CH_4, H_2, H_2O, CO and CO_2 as fuel, have been discussed. The computational domain comprises of nine subdomains, namely the anode and cathode interconnects, fuel and air channels, anode and cathode electrode diffusion and catalyst layers, and the electrolyte. The generality of the PDEs, used to describe the physical and electrochemical phenomena during DIR-SOFC operation, allows them to be applied for any geometry, flow configuration or design and also for any fuel or oxidant composition. For the simulation of the mass transport phenomena the combination of the SMM and the DGM formulation, that was presented and validated in [21, 22] was employed. The commercial FEM-based PDE solver, COMSOL Multiphysics [36], was used for the solution and postprocessing of the DIR-SOFC system. The MSR reaction is much slower than the WGS reaction; therefore its reaction rate was based on a kinetic approach, while the WGS reaction rate was based on an equilibrium assumption [10]. Other unique features of this model are that it uses composite electrodes configuration, allowing the representation of the TPBs by finite 2-D subdomains rather than 1-D boundaries, and that both H_2 and CO electrochemical oxidation reactions are taken into account in the current density computation.

In this work, the mechanisms of coupled transport and chemical/electrochemical reactions phenomena in the porous electrodes were studied and suggestions for improvement of the DIR-SOFC performance were discussed. Species compositions, temperature, ionic and electronic, as well as current density distribution results were obtained and presented. The performed simulations indicated a strong cooling effect at the anode electrode near the inlet, due to the highly endothermic MSR reaction. The formation of thermal gradients, associated with the endothermic behavior of the MSR reaction and the exothermic behavior of the WGS and electrochemical reactions at different locations, sets a limitation on the amount of reforming allowed in practice, since the mechanical integrity and reliability implications have to be taken into account by evaluating the thermal stresses imposed on the structure. Polarization curves were also generated to evaluate the effect of various design and

operating parameters on the DIR-SOFC performance. Parametric investigation showed that the performance of the DIR-SOFC, with respect to its power output predicted by the polarization curves, can be improved by higher temperature operation, since the increase in temperature has a decreasing effect on the DIR-SOFC overpotentials. On the other hand, it was shown that decreasing the inlet temperature leads to smoother temperature profiles and to the formation of smaller thermal gradients. Although the DIR-SOFC performance was found to be affected by the thickness of the electrochemically active anode catalyst layer, the net system response was found to be not substantially affected at the conditions simulated, due to the counter-balancing behavior of the ohmic and activation overpotentials. Electronic and ionic potentials distributions were also presented across the solid structure thickness, which enable the individual evaluation of the activation, concentration and ohmic overpotential terms.

Although further experimental data are required to validate the developed model for a wider range of operating conditions and design parameters, the detailed modeling framework presented here can be used for DIR-SOFC design and optimisation purposes, as well as a tool to provide better understanding of the complex interrelated processes taking place in an DIR-SOFC.

All research data supporting this publication are directly available within this publication.

References

[1] W. Lehnert, J. Meusinger, F. Thom, *Journal of Power Sources* **2000**, *87*, 57.

[2] S. Douvartzides, F. Coutelieris, P. Tsiakaras, *Journal of Power Sources* **2004**, *131*, 224.

[3] R. J. Braun, *Ph.D. Thesis*, University of Wisconsin – Madison, Madison Wisconsin, USA, **2002**.

[4] J. Laurencin, B. Morel, Y. Bultel, F. Lefebvre-Joud, *Fuel Cells* **2006**, *6*, 64.

[5] R. Bove, S. Ubertini, *Journal of Power Sources* **2006**, *159*, 543.

[6] K. Kanamura, S. Yoshioka, Z.-i. Takehara, *Journal of The Electrochemical Society* **1991**, *138*, 2165.

[7] T. Aloui, K. Halouani, *Applied Thermal Engineering* **2007**, *27*, 731.

[8] M. J. Lampinen, M. Fomino, *Journal of The Electrochemical Society* **1993**, *140*, 3537.

[9] M. Sommer, A. Lamm, A. Docter, D. Agar, *Journal of Power Sources* **2004**, *127*, 313.

[10] P. Aguiar, C. S. Adjiman, N. P. Brandon, *Journal of Power Sources* **2004**, *138*, 120.

[11] D. Sanchez, R. Chacartegui, A. Munoz, T. Sanchez, *International Journal of Hydrogen Energy* **2008**, *33*, 1834.

[12] K. Nikooyeh, A. A. Jeje, J. M. Hill, *Journal of Power Sources* **2007**, *171*, 601.

[13] I. K. Kookos, *Chemical Engineering Science* **2012**, *69*, 571.

[14] R. Suwanwarangkul, E. Croiset, M. W. Fowler, P. L. Douglas, E. Entchev, M. A. Douglas, *Journal of Power Sources* **2003**, *122*, 9.

[15] V. Novaresio, M. García-Camprubí, S. Izquierdo, P. Asinari, N. Fueyo, *Computer Physics Communications* **2012**, *183*, 125.

[16] Y. Vural, L. Ma, D. B. Ingham, M. Pourkashanian, *Journal of Power Sources* **2010**, *195*, 4893.

[17] V. M. Janardhanan, O. Deutschmann, *Journal of Power Sources* **2007**, *162*, 1192.

[18] V. M. Janardhanan, O. Deutschmann, *Chemical Engineering Science* **2007**, *62*, 5473.

[19] H. Zhu, R. J. Kee, V. M. Janardhanan, O. Deutschmann, D. G. Goodwin, *Journal of the Electrochemical Society* **2005**, *152*, A2427.

[20] F. Priyakorn, N. Laosiripojana, S. Assabumrungrat, *Journal of Sustainable Energy & Environment* **2011**, *2*, 187.

[21] K. Tseronis, I. K. Kookos, C. Theodoropoulos, *Chemical Engineering Science* **2008**, *63*, 5626.

[22] K. Tseronis, I. Bonis, I. K. Kookos, C. Theodoropoulos, *International Journal of Hydrogen Energy* **2012**, *37*, 530.

[23] I. Bonis, C. Theodoropoulos, *Chemical Engineering Science* **2012**, *69*, 69.

[24] E. Luna-Ortiz, C. Theodoropoulos, *Multiscale Modeling & Simulation* **2005**, *4*, 691.

[25] I. Bonis, W. Xie, C. Theodoropoulos, *AIChE Journal* **2012**, *58*, 801.

[26] W. Xie, I. Bonis, C. Theodoropoulos, *Computers & Chemical Engineering* **2011**, *35*, 750.

[27] J. Pallson, *Ph.D. Thesis*, Lund University, Lund, Sweden, **2002**.

[28] P. Aguiar, D. Chadwick, L. Kershenbaum, *Chemical Engineering Science* **2002**, *57*, 1665.

[29] S. Park, R. J. Gorte, J. M. Vohs, *Applied Catalysis A: General* **2000**, *200*, 55.

[30] Y. Kim, J. H. Kim, J. Bae, C. W. Yoon, S. W. Nam, *Journal of Physical Chemistry* **2012**, *116*, 13281.

[31] W. Wang, C. Su, Y. Wu, R. Ran, Z. Shao, *Chemical Reviews* **2013**, *113*, 8104.

[32] P. Iora, P. Aguiar, C. S. Adjiman, N. P. Brandon, *Chemical Engineering Science* **2005**, *60*, 2963.

[33] R. T. Leah, N. P. Brandon, P. Aguiar, *Journal of Power Sources* **2005**, *145*, 336.

[34] A. L. Dicks, *Journal of Power Sources* **1998**, *71*, 111.

[35] F. Mueller, J. Brouwer, F. Jabbari, S. Samuelsen, *Journal of Fuel Cell Science and Technology* **2006**, *3*, 144.

[36] COMSOL, COMSOL Multiphysics 3.3 – User's Guide, COMSOL AB, **2007**.

[37] S. B. Adler, J. A. Lane, B. C. H. Steele, *Journal of the Electrochemical Society* **1996**, *143*, 3554.

[38] S. B. Adler, *Chemical Reviews* **2004**, *104*, 4791.

[39] V. M. Janardhanan, V. Heuveline, O. Deutschmann, *Journal of Power Sources* **2008**, *178*, 368.

[40] M. Cannarozzo, S. Grosso, G. Agnew, A. Del Borghi, P. Costamagna, *Journal of Fuel Cell Science and Technology* **2007**, *4*, 99.

[41] J.-W. Kim, A. V. Virkar, K.-Z. Fung, K. Mehta, S. C. Singhal, *Journal of the Electrochemical Society* **1999**, *146*, 69.

[42] E. Achenbach, E. Riensche, *Journal of Power Sources* **1994**, *52*, 283.

[43] V. D. Belyaev, T. I. Politova, O. A. Mar'ina, V. A. Sobyanin, *Applied Catalysis A: General* **1995**, *133*, 47.

[44] H. Yakabe, T. Ogiwara, M. Hishinuma, I. Yasuda, *Journal of Power Sources* **2001**, *102*, 144.

[45] K. Ahmed, K. Föger, *Journal of Power Sources* **2001**, *103*, 150.

[46] H.-K. Park, Y.-R. Lee, M.-H. Kim, G.-Y. Chung, S.-W. Nam, S.-A. Hong, T.-H. Lim, H.-C. Lim, *Journal of Power Sources* **2002**, *104*, 140.

[47] D. F. Cheddie, N. D. H. Munroe, *Journal of Power Sources* **2006**, *160*, 215.

[48] D. F. Cheddie, N. D. H. Munroe, *The International Journal of Transport Phenomena* **2006**, *8*, 51.

[49] J. R. Welty, C. E. Wicks, R. E. Wilson, G. Rorrer, *Fundamentals of Momentum, Heat and Mass Transfer*, 4th Ed., John Wiley & Sons, **2000**.

[50] J. Y. Ofori, S. V. Sotirchos, *Industrial & Engineering Chemistry Research* **1996**, *35*, 1275.

[51] R. Taylor, R. Krishna, *Multicomponent Mass Transfer*, 1st Ed., John Wiley & Sons, **1993**.

[52] A. Runstedtler, *Chemical Engineering Science* **2006**, *61*, 5021.

[53] E. A. Mason, A. P. Malinauskas, *Gas Transport in Porous Media: The Dusty-Gas Model*, Elsevier, **1983**.

[54] R. Jackson, *Transport in Porous Catalysts*, 1st Ed., Elsevier, **1977**.

[55] Y. Matsuzaki, I. Yasuda, *Journal of the Electrochemical Society* **2000**, *14*, 1630.

[56] J. Vandersteen, B. Kenney, J. G. Pharoah, K. Karan, paper presented in: Hydrogen and Fuel Cell Conference, Canada, **2004**.

[57] D. Cheddie, N. Munroe, *Journal of Power Sources* **2006**, *156*, 414.

[58] Y. Shi, N. Cai, C. Li, *Journal of Power Sources* **2007**, *164*, 639.

[59] P. T. Nguyen, T. Berning, N. Djilali, *Journal of Power Sources* **2004**, *130*, 149.

[60] M. M. Hussain, X. Li, I. Dincer, *International Journal of Energy Research* **2005**, *29*, 1083.

[61] M. Suzuki, N. Shikazono, K. Fukagata, N. Kasagi, *Journal of Power Sources* **2008**, *180*, 29.

[62] L. Andreassi, G. Rubeo, S. Ubertini, P. Lunghi, R. Bove, *International Journal of Hydrogen Energy* **2007**, *32*, 4559.

[63] G. Wang, Y. Yang, H. Zhang, W. Xia, *Journal of Power Sources* **2007**, *167*, 398.

[64] J. Udagawa, P. Aguiar, N. P. Brandon, *Journal of Power Sources* **2007**, *166*, 127.

[65] M. M. Hussain, X. Li, I. Dincer, *Journal of Power Sources* **2006**, *161*, 1012.

[66] A. Chaisantikulwat, C. Diaz-Goano, E. S. Meadows, *Computers & Chemical Engineering* **2008**, *32*, 2365.

[67] H. S. Fogler, *Elements of Chemical Reaction Engineering*, 3rd Ed., Prentice Hall, New Jersey, **1999**.

[68] E. N. Fuller, J. C. Giddings, *Journal of Gas Chromatography* **1965**, *3*, 222.

[69] R. E. Cunningham, R. J. J. Williams, *Diffusion in Gases and Porous Media*, 1st Ed., Plenum Press, New York, **1980**.

[70] J. Liu, S. A. Barnett, *Solid State Ionics* **2003**, *158*, 11.

[71] P. Chinda, S. Chanchaona, P. Brault, W. Wechsatol, *The European Physical Journal – Applied Physics* **2011**, *54*, 23405.

[72] M. Ni, M. K. H. Leung, D. Y. C. Leung, *Energy Conversion and Management* **2007**, *48*, 1525.

[73] M. M. Hussain, X. Li, I. Dincer, *Journal of Power Sources* **2009**, *189*, 916.

————————————————